RSC Advances

PAPER

View Article Online
View Journal | View Issue

Cite this: *RSC Adv.*, 2019, **9**, 7645

High-temperature stability of nanozirconate-toughed IMF material lanthanum synthesized by an *in situ* reaction

Xin Wang, *[a] Min Xue,[a] Songbai Liu,[a] Kuo Jiang[a] and Zhuli Zhang[b]

Received 19th November 2018
Accepted 31st January 2019

DOI: 10.1039/c8ra09501a

rsc.li/rsc-advances

Herein, powders composed of $La_2Zr_2O_7$ (LZ) and ZrO_2 phases were synthesized by an *in situ* reaction using a sol-spray pyrolysis method; moreover, 24 mol% $LaO_{1.5}$–ZrO_2 (volume ratio = 1 : 1) powders were characterized by XRD, Raman spectroscopy, SEM, and TEM. XRD and Raman results showed that the samples maintained a tetragonal ZrO_2 and a pyrochlore LZ phase from 900 to 1100 °C. The addition of LZ could be helpful in the stabilization of t-ZrO_2 and decreasing the grain size of ZrO_2. The SEM results revealed that the LZ and ZrO_2 phases were homogeneously distributed in the sintered bulk. The HRTEM results suggested that the crystal orientations of the nano-LZ and nano-ZrO_2 phases were accordant; this was in agreement with the characteristics of the coherent boundaries. The fracture toughness of LZ–ZrO_2 was markedly improved by the transformation toughening of the ZrO_2 phase, and a value that was 2.2-fold that of the LZ prepared by a similar technique was achieved.

1. Introduction

In inert matrix (IM) materials, plutonium is inlaid in a U-free matrix; hence, plutonium can be burnt without breeding any new plutonium by neutron capture in ^{238}U. The basic criteria for IM materials are as follows: (i) stable irradiation behavior; (ii) good heat transport properties and phase stability at high working temperatures; and (iii) suitable mechanical properties such as elastic constants, fracture toughness and so on.[1–4] $La_2Zr_2O_7$ (LZ) with a pyrochlore (P) structure is one of the most evaluated potential IM materials because of its good stable irradiation behavior and phase stability at high working temperatures.[5,6]

However, the low thermal conductivity and fracture toughness of LZ has limited its applications in a fuel cycle that relies on a reprocessing strategy. The use of higher-thermal-conductivity materials (such as MgO and CeO_2) as a dual phase is a general method to improve the thermal conductivity of the IM materials.[7,8] However, only a few studies have been reported on the toughening of LZ. The incorporation of zirconia (ZrO_2) with high toughness into alumina ceramics to deliberately toughen them has been widely carried out to achieve zirconia-toughened alumina (ZTA) systems.[9,10] Herein, ZrO_2 has been incorporated into LZ to toughen it. Moreover, ZrO_2 has a relatively high thermal conductivity with additional excellent radioactive resistance and good mechanical properties.[11,12] The tetragonal (t)–monoclinic (m) transition of zirconia is believed to easily occur at temperatures less than 1150 °C.[13] This phase transition accompanying a change in the exterior environment induces a volume dilation of ~4 vol%. The stresses resulting from the volumetric changes can induce crack openings and thus limit the application of zirconia.[14]

Nanosized materials have relatively low activation energy for grain-boundary migration because of the increased surface (interface)/volume ratio as compared to their bulk counterparts.[15,16] For nanozirconia, when the crystallite size is ~30 nm or less, this phase transition occurs slowly. Moreover, nanocrystalline materials have a superior radiation resistance.[17]

The use of second-phase particles causes a grain-boundary motion by drag and can retard the grain growth of the matrix particles. It was reported that less than 1 mol% $LaO_{1.5}$ could be dissolved in ZrO_2.[18,19] Based on the phase diagram of the $LaO_{1.5}$–ZrO_2 system and the previous study, a pyrochlore-structured LZ phase exists in a wide concentration range of $LaO_{1.5}$. The phase composition of the $xLaO_{1.5} - (1-x)ZrO_2$ ($x \leq 1$) system at room temperature consists of LZ and ZrO_2 with the following chemical formula:

$$(1-x)LaO_{1.5} + xZrO_2 \rightarrow (1-x)/2La_2Zr_2O_7 + (2x-1)ZrO_2 \quad (1)$$

Soft solution chemistry, such as a sol–gel method, has been used to fabricate lanthanum zirconate and yttria-stabilized zirconia.[20] It provides a possible route for the production of nanocrystalline LZ and nanocrystalline ZrO_2 compounds in the nanometer scale. As a result, the grain size of ZrO_2 or LZ in the composite will be smaller than that of the single-phase

[a]*Department of Defence Science and Technology, Southwest University of Science and Technology, Mianyang 621010, China. E-mail: xinwang@swust.edu.cn*
[b]*Suzhou InReal Optoelectronic Material Technology Co., Ltd., China*

counterparts. It is suggested that the stabilization of t-ZrO_2 in the $LaO_{1.5}$–ZrO_2 system may result from the impact of the LZ phase.

The objectives are to (i) prepare nano–nano LZ–ZrO_2 composite powders by an *in situ* reaction using a sol-spray pyrolysis method, (ii) measure the toughness of LZ–ZrO_2, and (iii) study the high-temperature stability of LZ–ZrO_2; this provides a method to toughen not only LZ, but also all other pyrochlore IM materials (such as $Pu_2Zr_2O_7$ (ref. 21) and $Nd_2Zr_2O_7$ (ref. 8)); this will benefit the emerging area of IM research related to alternate ceramics.

2. Experimental procedures

2.1. Sample preparation

For the preparation of the LZ–ZrO_2 nanocomposite powders, 99.99% purity $Zr(NO_3)_4\cdot 3H_2O$ and $La(NO_3)_3\cdot 6H_2O$ (Aladdin Chemistry Co., Ltd., Shanghai, China) were used as the starting materials and dissolved in deionized water; the concentration of Zr^{4+} and La^{3+} was 0.1 M. In the starting solution, citric acid ($C_6H_8O_7\cdot H_2O$, 80 g L^{-1}) and polyethylene glycol (PEG, molecular weight = 20 000, 50 g L^{-1}) were used as the chelating agent and the plastering agent, respectively. The solution was stirred using a magnetic stirrer for 30 min to achieve complete dissolution. The resultant solution was then poured into a polytetrafluoroethylene (PTFE) tube and atomized by a stainless steel nozzle. Then, the precursors obtained from the sol-spray pyrolysis were annealed at 900–1200 °C for 6 h in high-purity Al_2O_3 crucibles and cooled down to room temperature (heating and cooling rates = 2 °C min^{-1}). To obtain dense samples, the powders were heated under an applied pressure of 40 MPa to 1450 °C at the constant heating rate of 100 min^{-1} for 10 min and rapidly cooled down to room temperature. All the bulk samples prepared in this study had a diameter of 15 mm and a height of approximately 5 mm. The bulk samples were polished using a 0.025 μm diamond paste and thermally etched at 1200 °C for 10 h in air. The density of the samples was determined by the Archimedes method.

2.2. Characterization of the sample composition and microstructure

X-ray diffraction (XRD) analysis of the samples was carried out using the X'Pert PRO diffractometer with Cu Kα radiation (λ = 0.15406 nm; PANalytical, Almelo, the Netherlands). The XRD patterns were obtained in the 2θ range of 10–90° at room temperature at the scanning rate of 0.05° s^{-1} and a step size of 0.033°. The crystallite size was calculated using the Scherrer's formula for the 440, 220 and 111 peaks of $La_2Zr_2O_7$, t-ZrO_2, and m-ZrO_2, respectively:

$$D = \frac{0.89\lambda}{(\beta_{obs} - \beta_{std})\cos\theta} \quad (2)$$

where D is the crystallite size (nm), λ is the wavelength (nm), β_{obs} is the FWHM, β_{obs} is the instrumental broadening parameters (0.05°), and θ is the diffraction angle.

Raman spectra were obtained using the Renishaw InVia Raman spectrometer (Renishaw plc, New Mills, UK). The emission line at 514.5 nm obtained from an Ar^+ ion laser was used as the excitation source. The samples of the bulk were observed using a field emission scanning electron microscope (FESEM, Apollo 300 FE, Obducat CamScan Ltd., Cambridge, UK) operated at 30 kV. The TEM observation of the samples was conducted using a transmission electron microscope (TEM, JEM-2010, JEOL, Tokyo, Japan).

2.3. Characterization of the sample fracture toughness

A Vickers hardness tester (HV-1000A, Huayin Test Instrument Co., Ltd., Yantai, China) was used to measure the indentation fracture toughness. The indentations were made on polished surfaces with a load (F) of 9.8 N held for 10 s. The fracture toughness (K_{IC}, MPa $m^{1/2}$) for each sample was estimated from a minimum of 9 indents to reduce the experimental uncertainty using the following equation:[22,23]

$$K_{IC} = 0.16 \times H_V \times a^{1/2} \times \left(\frac{c}{a}\right)^{-3/2} \quad (c/a \geq 2.5) \quad (3)$$

where H_V is the hardness, a is half the diagonal length of the Vickers indent (μm), and c is the crack length measured from the indent center (μm). The values of a and c were measured using an SEM instrument.

3. Results and discussion

3.1. Characterization of the LZ–ZrO_2 powders

X-ray diffraction was employed to investigate the crystalline phases of lanthanum zirconate and zirconia. The XRD patterns of $xLaO_{1.5} - (1 - x)ZrO_2$ (x = 0–0.5) powders obtained after annealing the powders at 1200 °C for 6 h are shown in Fig. 1. In the pattern of pure ZrO_2, no clear evidence is found for the presence of the t and c peaks. The shifts of the (−111) and (111) peaks in the pattern of 1 mol% $LaO_{1.5}$–ZrO_2 are an indication

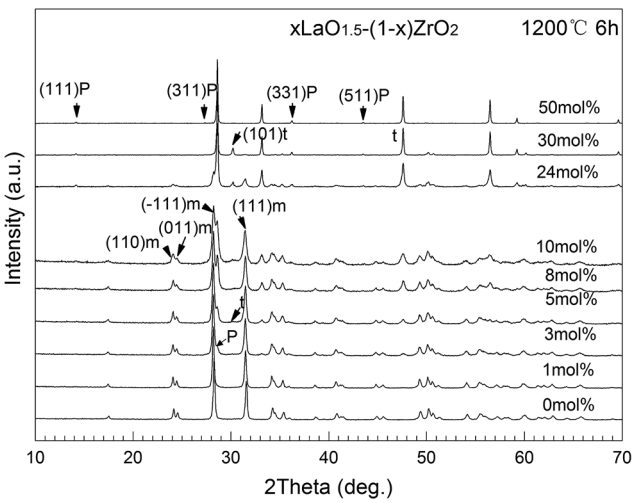

Fig. 1 XRD patterns of the $xLaO_{1.5} - (1 - x)ZrO_2$ (x = 0–50 mol%) powders after annealing at 1200 °C for 6 h in air.

that $LaO_{1.5}$ has been completely doped into the ZrO_2 crystal by substituting La^{3+} for Zr^{4+}. The presence of the pyrochlore structure is confirmed by the occurrence of the superlattice 311, 331, and 511 peaks.[24] The results indicate that the solubility of $LaO_{1.5}$ in ZrO_2 is lower than 1 mol%; this in line with that reported in literature.[18,19] The broadening of the m (111) peaks indicated that the grain size of m-ZrO_2 decreased with an increase in the content of LZ. Considering the grain size effect of ZrO_2, the presence of the (101) peak for t-ZrO_2 could be attributed to the grain refinement.

Table 1 summarizes the calculated grain sizes of m-ZrO_2 in $xLaO_{1.5} - (1 - x)ZrO_2$ (x = 0–0.4) powders after annealing at 1200 °C for 6 h. The data showed that the grain size of the m phase gradually decreased with the increasing concentration of $LaO_{1.5}$, reaching a value that was approximately equal to the critical grain size of t- to m-ZrO_2 at the addition concentration of 10 and 24 mol%. The (101) peak for t-ZrO_2 significantly increased at the concentration of 24 mol%. The lattice parameters of LZ and ZrO_2 were determined based on the XRD patterns shown in Fig. 1. The volume ratios of LZ and m-ZrO_2 in the samples could be easily calculated using the weight and the number of formula units per elementary cell, which were approximately 1/4, 1/1 and 4/1 for 10, 24 and 40 mol% $LaO_{1.5}$–ZrO_2 samples, respectively. The 24 mol% $LaO_{1.5}$–ZrO_2 powders were chosen for further characterization.

3.2. Fracture toughness

Fig. 2(a) shows the fracture surface of the 24 mol% $LaO_{1.5}$–ZrO_2 spark plasma sintered (SPS) bulk sample after thermal etching at 1100 °C for 2 h. The SEM image reveals that the particle size of the SPS bulk sample is in the range of 50–200 nm. The SEM image reveals that the sintered sample has a dense microstructure, which is very important for the mechanics performance testing. The densities of the sintered LZ and 24 mol% $LaO_{1.5}$–ZrO_2 specimens were determined by the Archimedes method to be 97.6% and 95.8% of the theoretical values, respectively.

Fig. 2(b) shows the fracture toughness of the 24 mol% $LaO_{1.5}$–ZrO_2 sample, and the data have been compared with that of the LZ materials. The experimental results for the LZ samples are in good agreement with those reported in the literature.[25] The data showed that the toughness level of the 24 mol% $LaO_{1.5}$–ZrO_2 was 120% greater than that of LZ (~1.0 MP $m^{1/2}$). The high fracture toughness of 24 mol% $LaO_{1.5}$–ZrO_2 (as compared to that of LZ) can be attributed to the transformation toughening from the martensitic transformation of the t to the m phases.

Table 1 The calculated crystallite sizes and phase composition of m-ZrO_2 in $xLaO_{1.5} - (1 - x)ZrO_2$ (x = 0–0.4) powders after annealing at 1200 °C for 6 h[a]

$LaO_{1.5}$ concentration (mol%)	Phase composition	Crystallite size of m-ZrO_2 (nm)
0	m	38.8
1	m	40.1
3	m + P	32.6
5	m + P+ t*	31.0
8	m + P + t*	28.1
10	m + P + t*	22.5
24	P + m + t	23.4
40	P + t + m*	—

[a] P – pyrochlore-type $La_2Zr_2O_7$; m – m-ZrO_2; t – t-ZrO_2; *small amount.

3.3. High-temperature stability and grain growth

Fig. 3 shows the XRD patterns of ZrO_2 and 24 mol% $LaO_{1.5}$–ZrO_2 powders after annealing at 500–1100 °C. Pure ZrO_2 presents clear t peaks at 500 °C. With an increase in the annealing temperature from 600 to 800 °C, pure ZrO_2 undergoes a t to m phase transformation. The grain size of the t phase was below 30 nm (see Table 2), in good agreement with the critical grain size for the t- to m-ZrO_2 transformation.[26] Compared with the case of pure ZrO_2, no clear evidence was found for the shift of the t (101) peaks in any of the patterns of 24 mol% $LaO_{1.5}$–ZrO_2; this indicated that the solubility of La^{3+} in the ZrO_2 phase was negligible. Table 2 lists the grain sizes of ZrO_2 and 24 mol% $LaO_{1.5}$–ZrO_2 powders calculated from the Scherrer's formula on the basis of Fig. 3. For pure ZrO_2, the crystallite size of t-ZrO_2 increased from 9.1 to 26.4 nm as the temperature was increased from 500 to 800 °C, and t-ZrO_2 disappeared above 900 °C. The crystallite sizes of LZ and ZrO_2 in the 24 mol% $LaO_{1.5}$–ZrO_2 system gradually increased from 19.5 to 38.1 nm and from 8.7 to 38.5 nm as the annealing temperature was elevated from 900 to 1100 °C. When the addition concentration of $LaO_{1.5}$ reached 24 mol%, the critical grain size for the t to m phase transformation increased from ~20 to ~40 nm when the corresponding heat treatment temperature was increased from 600 to 1100 °C. The data showed that the addition of LZ could be helpful in decreasing the grain size of ZrO_2.

Raman spectroscopy is another useful technique that is generally used to investigate the structures of lanthanum zirconate and zirconia. Fig. 4 shows the Raman spectra of the 24 mol% $LaO_{1.5}$–ZrO_2 powders annealed at 800, 900, and 1100 °C and the P–LZ samples.[27] The bands at 298, 389, 494, 511, and 744 cm^{-1} were assigned to the $A_{1g} + E_g + 4F_{2g}$ Raman active vibration modes (gray arrows) of the P–LZ sample. The bands corresponding to the $A_{1g} + 3E_g$ modes (black arrows) of t-ZrO_2 were clearly observed at 273, 463, 600 and 646 cm^{-1} in the spectra of the 24 mol% $LaO_{1.5}$–ZrO_2 powders,[28] in good agreement with the XRD results.

Fig. 5(a) and 4(b) show the SEM images of the 24 mol% $LaO_{1.5}$–ZrO_2 bulk samples after sintering at 1300 °C for 48 h at different magnifications. Fig. 5(a) reveals that the samples have a homogeneous microstructure. The particle size distribution of the samples is shown in Fig. 5(c), and the observed grain size of the samples is in the range of 0.1–1.4 μm. Fig. 5(b) reveals that the crystal grains of the sample are near spheroidal in shape. The SEM image also shows that the grains of the sample are closely bonded with each other, and the interfaces between grains are legible. In a previous study on the nano–nano composites of lanthanum zirconate and yttria-stabilized zirconia,[20] the activation energy for the grain growth of LZ

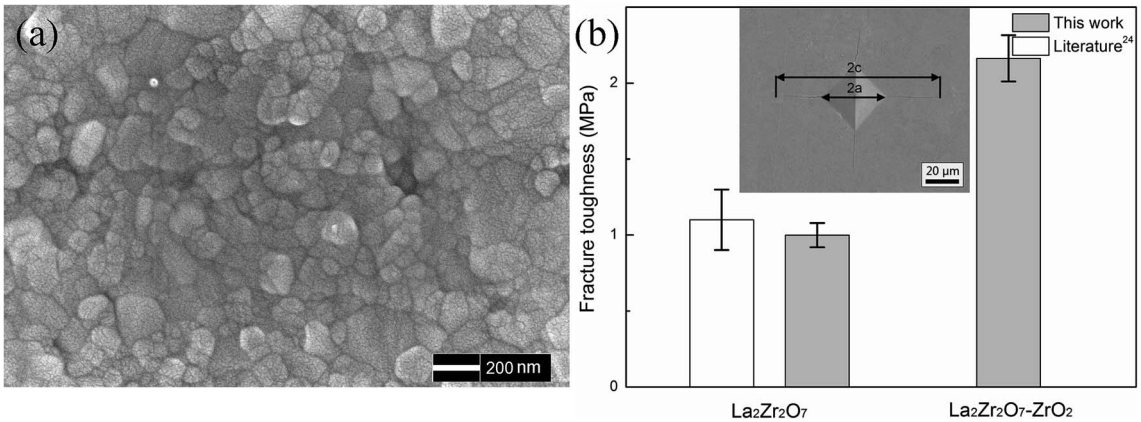

Fig. 2 (a) The SEM image of the 24 mol% $LaO_{1.5}$–ZrO_2 bulk sample. (b) Fracture toughness of the 24 mol% $LaO_{1.5}$–ZrO_2 and $La_2Zr_2O_7$ bulk samples. The data for $La_2Zr_2O_7$ is obtained from the study reported by Vassen *et al.*[25] Inset shows a Vickers indentation with cracks (polished, SEM, SE) by a 1 kg load of 24 mol% $LaO_{1.5}$–ZrO_2 ceramics.

(225 ± 12 kJ mol^{-1}) was much lower than that of 10YSZ (yttria-stabilized zirconia, 382 ± 17 kJ mol^{-1}); this suggested that the first step was the formation of LZ and nuclei, and then, ZrO_2 nucleated on the surface of the LZ crystalline grains during the annealing process. Therefore, the small crystals were the ZrO_2 nuclei, which were evenly distributed on the surface of the LZ nuclei *via* encircling and insertion.

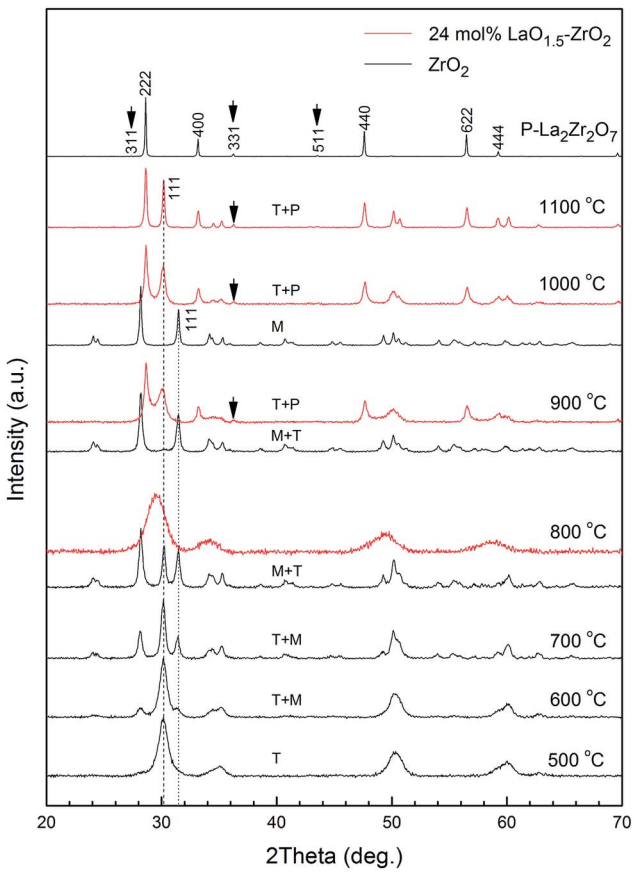

Fig. 3 XRD patterns of ZrO_2 and 24 mol% $LaO_{1.5}$–ZrO_2 powders after annealing at 500–1100 °C for 6 h.

To rationalize these results, the phase transformation mechanism of ZrO_2 was considered. Pure zirconia has three polymorphs under ordinary pressure, and the monoclinic type is the most frequent structure at room temperature and up to 1170 °C. In our case, pure ZrO_2 and ZrO_2 coexisting in the composite powders possess the t phase at 500 °C and 800–1100 °C, as confirmed by the XRD measurements. The appearance of the high-temperature phase at low temperatures has been discussed, and Parija *et al.*[29] have proposed that the main reason for the stabilization is the crystallite size effect. According to their opinion, the following equation for the radius of the critical crystallite size r_c for the t–m transformation has been proposed:

$$r_c = -3\Delta\sigma/[q(1 - T/T_b) + \Delta\varepsilon] \quad (4)$$

where $\Delta\varepsilon$ is the change in the strain energy/unit volume for a particle, q is the heat of the t–m transformation, $\Delta\sigma$ is the difference between the surface-free energies of the m and t phases of ZrO_2, T_b is the temperature at which the t–m transformation occurs for ZrO_2 (1170 °C), and T is the temperature at which the crystallites of a given radius r_c undergo the t–m transformation. At room temperature, the following parameter values were used for the calculation of r_c: $\Delta\sigma = 0.91$ J m^{-2}, $q =$

Table 2 The calculated crystallite sizes for ZrO_2 and 24 mol% $LaO_{1.5}$–ZrO_2 after annealing at 500–1100 °C for 6 h

	Crystallite size (nm)			
	ZrO_2		24 mol% $LaO_{1.5}$–ZrO_2	
Sample (°C)	t	m	t	P
500	9.1	—	—	—
600	11.2	—	—	—
700	21.3	24.9	—	—
800	26.4	24.8	—	—
900	—	29.9	8.7	19.5
1000	—	42.9	16.9	24.1
1100	—	—	38.5	38.1

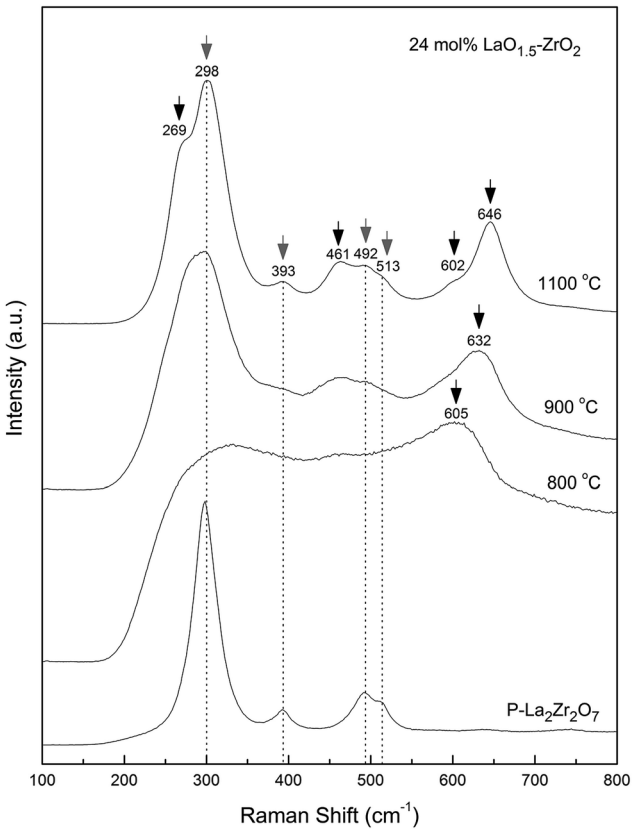

Fig. 4 Raman spectra of 24 mol% $LaO_{1.5}$–ZrO_2 powders after annealing at 800, 900, and 1100 °C for 6 h, and $La_2Zr_2O_7$.

-2.82×10^8 J m^{-1},[3] $T_b = 1443$ K, $T = 298$ K, and $\Delta\varepsilon = 0.46 \times 10^8$ J m^{-1}.[3] The value of r_c is *ca.* 15 nm.

The grain size of pure ZrO_2 presented in Table 1 corresponds well with the calculated r_c. Similar to that of 24 mol% $LaO_{1.5}$–ZrO_2, the t-ZrO_2 phase is stable even at the grain size of 38.5 nm. As indicated in eqn (3), the value of r_c depends on $\Delta\sigma$, q, T_b, T, and $\Delta\varepsilon$. In Fig. 2, no peak shift of the t and m phases was observed for all the samples; this indicated that La was not doped into the ZrO_2 crystal. This suggests that the values of $\Delta\sigma$ and q are consistent with those of pure ZrO_2. T_b and T are constant; thus, the change in the strain energy may be the main factor for the increased r_c.

In the Raman spectra (Fig. 4), a significant shift ($\sim$14 cm^{-1}) towards lower frequencies for t-ZrO_2 was observed in the range of 600–650 cm^{-1} with a decrease in the annealing temperature from 1100 to 900 °C. Djurado *et al.*[26] reported that the grain size effect on the Raman spectra was much smaller than the pressure-induced effect, and the maximum shift value was less than 10 cm^{-1}. This suggests that stress exists in the $LaO_{1.5}$–ZrO_2 composite samples. Furthermore, the SEM images (Fig. 5(b)) show that small ZrO_2 particles are embedded into the large LZ particles. In other words, the ZrO_2 particles grew at the grain boundary.

To confirm the grain-boundary growth, high-resolution TEM characterization was performed. Fig. 6 shows a TEM image of the 24 mol% $LaO_{1.5}$–ZrO_2 powders after annealing at 1000 °C for 6 h. The lattice fringes with 0.620 and 0.315 nm spacings can be assigned to the 111 lattice plane of pyrochlore–LZ (P–LZ) and

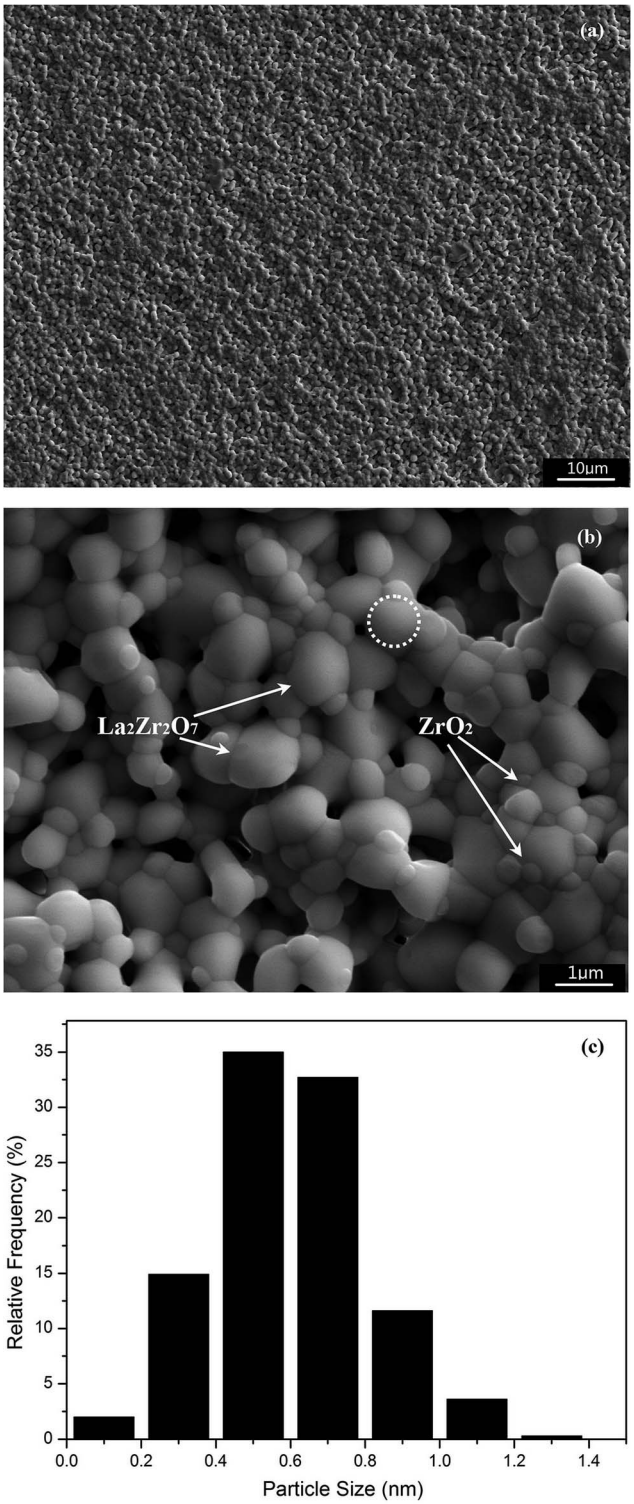

Fig. 5 (a) and (b) SEM images of 24 mol% $LaO_{1.5}$–ZrO_2 bulk samples after sintering at 1300 °C for 48 h, and (c) particle size distribution of the 24 mol% $LaO_{1.5}$–ZrO_2 bulk sample obtained from the SEM images.

the 111 lattice plane of t-ZrO_2 phase, respectively. The TEM image shows that the ZrO_2 crystal grows along the surface of the LZ crystal, and the crystal orientation of the two phases is accordant, in line with the characteristics of coherent boundaries. The coherent boundaries with low excess energies are

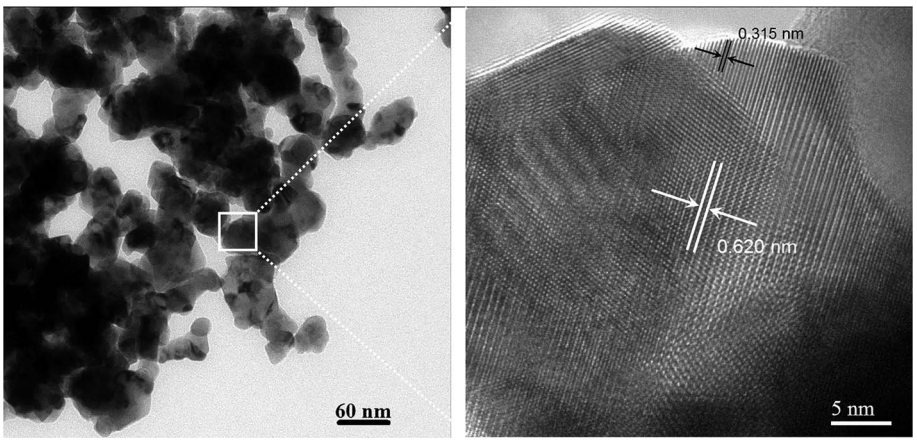

Fig. 6 TEM images of 24 mol% $LaO_{1.5}$–ZrO_2 powders after annealing at 1000 °C for 6 h.

believed to retard the grain growth of the matrix particles because the grain growth of nanosized materials is controlled by the grain-boundary migration. Hence, the stabilization mechanism of the t-ZrO_2 phase of the LZ–ZrO_2 composite powders should be attributed to the grain refinement and lattice stress effects.

Based on the abovementioned analysis, the lowest entropy will be selected during the *in situ* reaction. A possible mechanism for the formation of the $LaO_{1.5}$–ZrO_2 nano–nano composite powders has been suggested as follows: the first step is the formation of LZ and nuclei, and then, ZrO_2 nucleates on the surface of LZ crystalline grains during the annealing process.

4. Conclusions

In summary, the addition of $LaO_{1.5}$ to ZrO_2 forms a pyrochlore structural $La_2Zr_2O_7$ phase and induces a tetragonal to monoclinic (t to m) phase transition of ZrO_2. The addition of LZ could be helpful in stabilizing t-ZrO_2 and decreasing the grain size of ZrO_2. The t-ZrO_2 phase in the 24 mol% $LaO_{1.5}$–ZrO_2 powders was phase-stable up to a calcination temperature of 1100 °C. Since the solubility of $LaO_{1.5}$ in ZrO_2 is lower than 1 mol%, the presence of the t-ZrO_2 phase in the $LaO_{1.5}$–ZrO_2 system does not arise from doping stabilization by the substitution of La^{3+} for Zr^{4+}, but rather from the grain refinement of the LZ phase. The crystal orientation of the nano-LZ and nano-ZrO_2 phases was accordant, in line with the characteristics of the coherent boundaries. The fracture toughness of $La_2Zr_2O_7$–ZrO_2 has been markedly improved by the transformation toughening of the ZrO_2 phase, reaching a value that is 2.2-fold that of $La_2Zr_2O_7$ prepared by a similar technique.

Conflicts of interest

There are no conflicts to declare.

Acknowledgements

We thank Dr Ruishi Xie, Dr Zhaohui Zhou, and Dr Huiping Duan for assistance with XRD, SEM, and TEM. This work was supported by the project of NSFC-11505146 and Defense Industrial Technology Development Program JCKY2016404C001 and Longshan Academic Talent Research Supporting Program of SWUST 18LZX556.

References

1 H. Matzke, V. V. Rondinella and T. Wiss, *J. Nucl. Mater.*, 1999, **274**, 47–53.
2 C. Degueldre and J. M. Paratte, *J. Nucl. Mater.*, 1999, **274**, 1–6.
3 S. Lutique, D. Staicu, R. J. M. Konings, V. V. Rondinella, J. Somers and T. Wiss, *J. Nucl. Mater.*, 2003, **319**, 59–64.
4 R. Restani, M. Martin, N. Kivel and D. Gavillet, *J. Nucl. Mater.*, 2009, **385**, 435–442.
5 I. Hayakawa and H. Kamizono, *J. Nucl. Mater.*, 1993, **202**, 163–168.
6 S. Yamazaki, T. Yamashita, T. Matsui and T. Nagasaki, *J. Nucl. Mater.*, 2001, **294**, 183–187.
7 A. Imaura, N. Touran and R. C. Ewing, *J. Nucl. Mater.*, 2009, **389**, 341–350.
8 A. T. Nelson, M. M. Giachino, J. C. Nino and K. J. McClellan, *J. Nucl. Mater.*, 2014, **444**, 385–392.
9 N. Claussen, *J. Am. Ceram. Soc.*, 1976, **59**, 49–51.
10 D. J. Green, *J. Am. Ceram. Soc.*, 1982, **65**, 610–614.
11 C. Degueldre, T. Arima and Y. W. Lee, *J. Nucl. Mater.*, 2003, **319**, 6–14.
12 C. Ghosh, S. Sinhamahapatra and H. S. Tripathi, *Int. J. Appl. Ceram. Technol.*, 2018, **00**, 1–8.
13 R. Chaim, D. G. Brandon and A. H. Heuer, *Acta Metall.*, 1986, **34**, 1933–1939.
14 D. R. Clarke and C. G. Levi, *Annu. Rev. Mater. Res.*, 2003, **33**, 383–417.
15 W. P. Tong, N. R. Tao, Z. B. Wang, J. Lu and K. Lu, *Science*, 2003, **299**, 686–688.
16 K. Dick, T. Dhanasekaran, Z. Zhang and D. Meisel, *J. Am. Chem. Soc.*, 2002, **124**, 2312–2317.
17 S. Wurster and R. Pippan, *Scr. Mater.*, 2009, **60**, 1083–1087.
18 B. Bastide, P. Odier and J. P. Coutures, *J. Am. Ceram. Soc.*, 1988, **71**, 449–453.

19 M. A. Stough and J. R. Hellmann, *J. Am. Ceram. Soc.*, 2002, **85**, 2895–2902.
20 K. Jiang, S. Liu and C. Li, *J. Am. Ceram. Soc.*, 2013, **96**, 3296–3303.
21 R. Chawla, P. Grimm, P. Heimgartner, F. Jatuff, G. Ledergerber, A. Luthi, M. Murphy, R. Seiler and R. van Geemert, *Prog. Nucl. Energy*, 2001, **38**, 359–362.
22 A. G. Evans and E. A. Charles, *J. Am. Ceram. Soc.*, 1976, **59**, 371–372.
23 G. R. Anstis, P. Chantikul, B. R. Lawn and D. B. Marshall, *J. Am. Ceram. Soc.*, 1981, **64**, 533–538.
24 P. K. Schelling and S. R. Phillpot, *J. Am. Ceram. Soc.*, 2001, **84**, 2997–3007.
25 R. Vassen, X. Cao, F. Tietz, D. Basu and D. Stöver, *J. Am. Ceram. Soc.*, 2000, **83**, 2023–2028.
26 E. Djurado, P. Bouvier and G. Lucazeau, *J. Solid State Chem.*, 2000, **149**, 399–407.
27 D. Michel, M. P. y. Jorba and R. Collongues, *J. Raman Spectrosc.*, 1976, **5**, 163–180.
28 P. Bouvier and G. Lucazeau, *J. Phys. Chem. Solids*, 2000, **61**, 569–578.
29 A. Parija, G. R. Waetzig, J. L. Andrews and S. Banerjee, *J. Phys. Chem. C*, 2018, **122**, 25709–25728.